



ELSEVIER

Available online at [www.sciencedirect.com](http://www.sciencedirect.com)

SCIENCE @ DIRECT®

Journal of Computational and Applied Mathematics 183 (2005) 343–357

JOURNAL OF  
COMPUTATIONAL AND  
APPLIED MATHEMATICS

[www.elsevier.com/locate/cam](http://www.elsevier.com/locate/cam)

# Adaptive method of lines solutions for the extended fifth-order Korteweg–de Vries equation

P. Saucez<sup>a</sup>, A. Vande Wouwer<sup>b,\*</sup>, P.A. Zegeling<sup>c</sup>

<sup>a</sup>*Service de Mathématique et Recherche Opérationnelle, Faculté Polytechnique de Mons, Belgium*

<sup>b</sup>*Service d'Automatique, Faculté Polytechnique de Mons, Boulevard Dolez 31, Mons 7000, Belgium*

<sup>c</sup>*Mathematical Institute, Utrecht University, The Netherlands*

Received 13 May 2004; received in revised form 19 September 2004

## Abstract

In this paper, we investigate the dynamics and interaction properties of recently discovered “embedded solitons” in an extended fifth-order KdV model inspired by water waves in the presence of surface tension. The dynamical behaviour of the solitons can be efficiently followed by using a moving or an adaptive finite difference mesh in combination with a suitable time-integrator. We will demonstrate this numerically for different types of wave solutions, such as solitary waves, multihumped waves, and interacting waves.

© 2005 Elsevier B.V. All rights reserved.

*Keywords:* Solitary waves; Nonlinear dynamics; Water waves; Wave interaction; Adaptive mesh method; Finite differences; Method of lines

## 1. Introduction

In recent years, there has been considerable interest in the numerical treatment of partial differential equations (PDEs) describing nonlinear wave phenomena, and particular types of solitary waves. In this study, we focus our attention on an extended fifth-order Korteweg–de Vries (KdV) equation that can be used to model water waves with surface tension. The model is described by the PDE

$$u_t + \frac{2}{15} u_{xxxxx} + (\mu u - b)u_{xxx} + (3u + 2\mu u_{xx})u_x = 0 \quad (1)$$

\* Corresponding author. Tel.: +32 6537 4141; fax: +32 6537 4136.

*E-mail address:* [alain.vandewouwer@fpms.ac.be](mailto:alain.vandewouwer@fpms.ac.be) (A. Vande Wouwer).

for  $-\infty < x < \infty$ ,  $t > 0$ . In 1997, Champneys and Groves [2] studied the global existence properties of solitary wave solutions to Eq. (1), which can also be written in conservative form:

$$u_t + \left[ \frac{2}{15} u_{xxxx} - bu_{xx} + \left(\frac{3}{2}\right)u^2 + \mu\left(\frac{1}{2}\right)(u_x)^2 + (uu_x)_x \right]_x = 0. \quad (2)$$

This is a special case of a more general class of Hamiltonian evolution equations studied by Kichenassamy and Olver [10]. For  $\mu = 0$  this reduces to the usual fifth-order KdV equation introduced by Kawahara [9]. The extended form (1) may be derived via a regular Hamiltonian perturbation theory from an exact Euler equation formulation for water waves with surface tension [4]. Looking for traveling-wave solutions  $u(x - ct)$ , integrating once, setting the constant of integration to be zero, one arrives at the following ODE (the prime standing for  $d/d\xi$  with  $\xi := x + at$ ),

$$\frac{2}{15} u'''' - bu'' + au + \frac{3}{2} u^2 + \mu \left[ \frac{1}{2} (u')^2 + (uu')' \right] = 0, \quad (3)$$

where  $a := -c$ . Nonzero values of  $\mu$  can be scaled to plus or minus unity. For the rest of this work we shall take the sign value that is significant for water waves in the presence of surface tension and hence set  $\mu = 1$ . Physically,  $u(x, t)$  represents the height of the free surface of a 2D slab of fluid of finite depth. The parameter  $b$  and dimensionless wave speed  $a$  are related to the difference between the Bond and Froude numbers respectively from their critical values  $(\frac{1}{3}, 1)$ .

In this paper, we shall treat different cases for the parameters  $a$  and  $b$ . The first case with  $a < 0$  describes waves that travel to the right. This is of interest because any true solitary wave (i.e. homoclinic solution to the travelling-wave ODE (3) with exponentially decaying tails) must, according to Yang et al. [17,3,18], be an *embedded soliton* (ES) (note that the term “soliton” is used here in its physical rather than mathematical sense, since Eq. (1) is not completely integrable). That is, the solitary wave of the PDE (1) exists in resonance with the linear spectrum. This condition manifests itself in the travelling wave ODE (3) as the origin being of saddle-centre type, that is possessing both real and imaginary eigenvalues. Yang et al. [17] discovered by a formal energy argument in the context of a particular second-harmonic generation model from nonlinear optics that such solutions may be weakly stable linearly, but nonlinearly *semistable*. The semistability property states that an ES may be stable to perturbations which increase the solitary wave’s energy, but unstable to perturbations that reduce it. This interesting property can be verified with numerical experiments as we shall see in Section 2.

Recently Yang [16] discovered ESs in other generalised fifth-order KdV models, using soliton perturbation theory near various integrable limits. He also demonstrated with this technique that the simplest such solutions do indeed possess this semistability.

The aim of the present study is to undertake an in-depth numerical investigation into the properties of the ESs and other types of solitary waves existing in the particular form of extended fifth-order KdV equation (1). Specifically in [2,1] it was found numerically that there are a countable sequence of curves on which ESs exist; see Fig. 1. Note that only solutions on the uppermost curve could be described as “fundamental” ESs (i.e. having a single-humped shape). All other solutions, which appear to be fundamental as they tend to zero amplitude in the limit  $a \rightarrow 0$  for  $b < 0$ , increase in amplitude on increasing  $b$  and in so doing develop internal oscillations in their profiles (i.e. having a multihumped shape). See the insets to Fig. 1 which depict the profiles in the large-amplitude limit  $a \rightarrow 0$  with  $b > 0$ . Note that the small-amplitude limit is highly singular and the analytical determination of those values of  $b < 0$  leads to “bifurcations” of ES into the region  $a > 0$ . This is a subtle problem to analyse analytically (it is also a hard problem numerically, as witnessed by the solution loci ending short of the axis in the left-hand portion of Fig. 1).

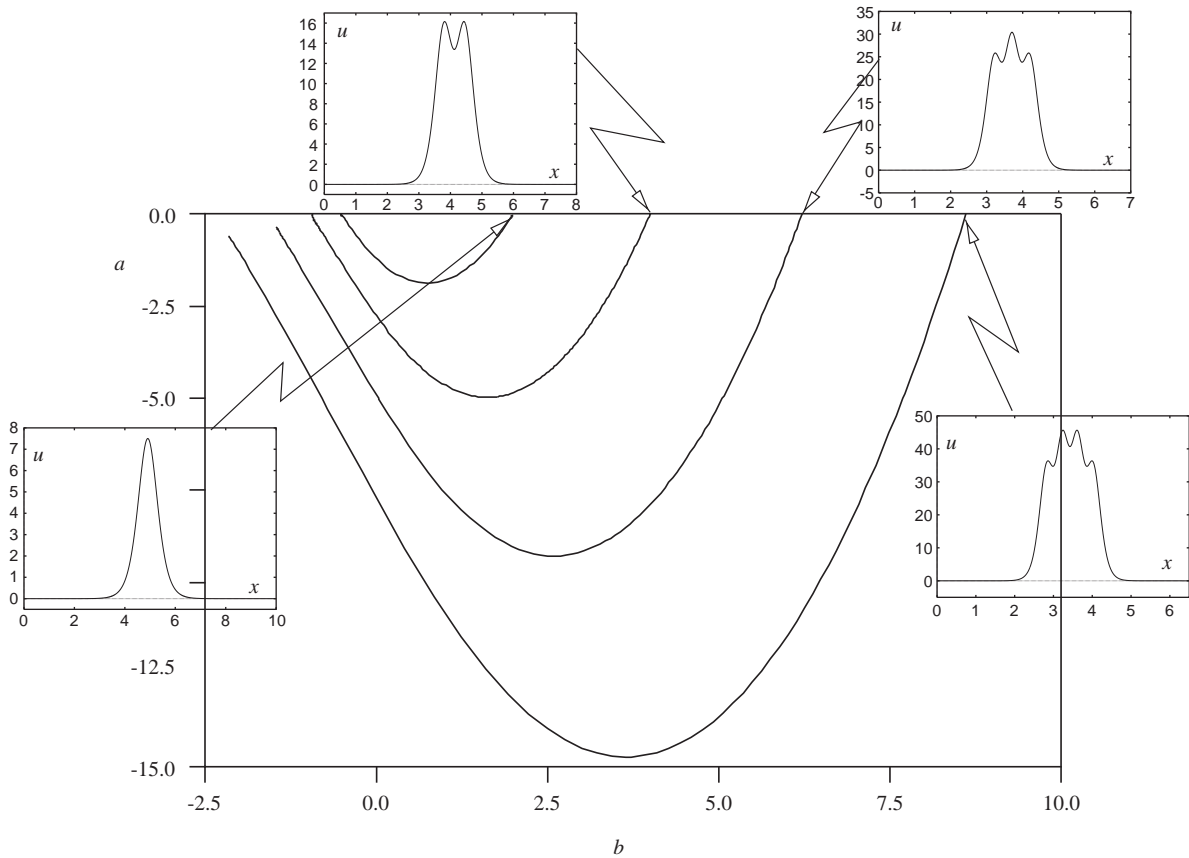


Fig. 1. The region of existence of the embedded solitons for Eq. (3) with  $\mu = 1$ .

Nevertheless, it is straightforward to determine that the fundamental wave bifurcates at  $b = -\frac{1}{2}$ , because in fact this solution is given by the explicit expression

$$u(x, t) = 3 \left( b + \frac{1}{2} \right) \operatorname{sech}^2 \left( \sqrt{\frac{3(2b+1)}{4}} (x + at) \right), \quad a = \frac{3}{5}(2b+1)(b-2), \quad b \geq -\frac{1}{2}. \quad (4)$$

We can recognize three different sub-cases depending on the sign of the parameter  $b$ :  $-\frac{1}{2} < b < 2$  the soliton moves from left to right,  $b = 2$  a motionless soliton and  $b > 2$  a soliton that moves to the left.

Note that this curve of exact solutions is also defined for  $a > 0$  ( $b > 2$ ) and indeed each of the numerically computed curves in Fig. 1 can be continued into  $a > 0$ . Here the solutions represent so-called *orbit-flip* solitary waves which exist inside a continuum of  $(a, b)$ -values at which there exist other solitary waves, but are distinguished by the faster rate of decay of their tails.

The layout of the paper is as follows. In the next section we present two different numerical approaches to the extended KdV5 model. The first one follows the solitons in a moving coordinate system, whereas the second method adapts the spatial mesh points to the solution profile itself. In Section 3 numerical experiments with the adaptive mesh method are shown for the case of embedded solitons, and also multihumped wave solutions. In Section 4 we present our conclusions.

## 2. Numerical methods

We shall employ two different numerical methods for PDE (1), both aiming at following the spatial and temporal profiles of the PDE solutions.

### 2.1. A uniformly moving mesh method

A rather straightforward technique can be constructed by making use of the constant speed  $-a$  of the solution as defined in (4) to define a moving (Lagrangian) co-ordinate system. This method is selected for its simplicity, but has strong limitations, i.e. it can only be used to follow a solution moving at constant speed in one direction.

#### 2.1.1. A moving co-ordinate transformation

We apply a co-ordinate transformation to the Eulerian co-ordinate system  $(x, t)$  of independent variables. For this purpose, we define  $\xi = \xi(x, t) = x + at, \theta = t$  to arrive at the Lagrangian co-ordinates  $(\xi, \theta)$ . Here,  $-a$  is the velocity of the moving frame which we shall take to be the speed  $-a$  of the ES under consideration. For the explicit solution (4),  $a$  is related to  $b$  by the given formula. Applying the transformation to PDE (1) and letting  $U(\xi, \theta)$  denote the dependent variable in the new co-ordinates yields

$$U_\theta + aU_\xi + \frac{2}{15} U_{\xi\xi\xi\xi\xi} + (\mu U - b)U_{\xi\xi\xi} + (3U + 2\mu U_{\xi\xi})U_\xi = 0. \tag{5}$$

The reason for re-writing the PDE is a numerical one, and can be simply illustrated by the following example. In Fig. 2 (left plot) two numerical solutions are shown in both co-ordinate systems for the

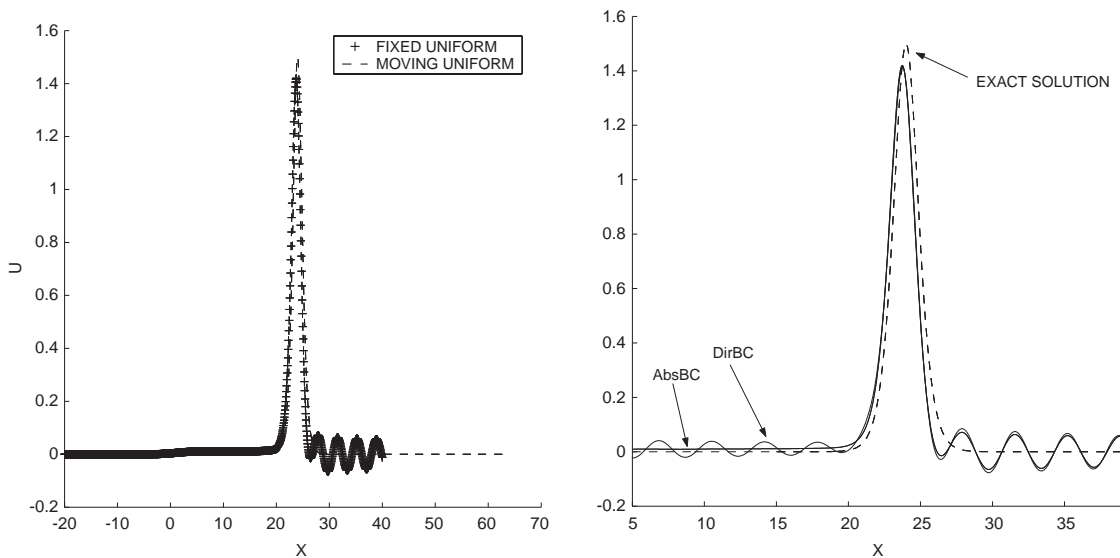


Fig. 2. Fixed uniform mesh vs. moving uniform mesh results (left) with 1001 meshpoints,  $b = 0$ , at  $t = 20$ . In the right plot we see clearly the effect of absorbing (“AbsBC”) vs. nonabsorbing BCs (“DirBC”).

same number of mesh points in the spatial direction and the same initial data, given by (4). It is clearly seen that the solution on a moving uniform mesh is superior to the fixed uniform mesh solution, since the numerical approximation follows the soliton “exactly” with the right speed. The fixed uniform mesh method produces unnatural oscillations at the right foot of the soliton, which further on in the computations will cause a breakdown of the method. It must be noted that the above-described approach can only be used for motion in one direction. For waves or solitons that, for example, develop in different directions, or that move with different speeds, more sophisticated methods have to be applied, such as solution-adaptive mesh techniques (see [5,19,20,14,12]). Such a method will be discussed in Section 2.2.

### 2.1.2. Boundary conditions

For the numerical solution of the PDE model, we need to impose boundary conditions at finite distance from the soliton, i.e. at both endpoints  $x = x_L$  and  $x = x_R$ . Since we take our boundaries “far away” from the soliton, it could be tempting to take merely zero conditions for  $U$  and its first derivatives at each end. However, since we would like to investigate the long-time behaviour of the soliton, and, in some cases, we add “noise” to investigate the stability properties, it is better to use so-called absorbing- or transport boundary conditions. Ideally, absorbing conditions let the incoming wave, pulse, or radiation go through the boundary, without reflection that could break up the numerical PDE solution later on in the computation. A first-order transport (or absorbing) condition (see [13]) can be described by

$$u_t + c_g u_x = 0, \quad (6)$$

where  $c_g$  stands for the group velocity of the expected disturbance. In the moving co-ordinate system this condition transforms into

$$U_\theta + (c_g + a)U_\xi = 0. \quad (7)$$

In our numerical experiments we expect the group velocity of the incoming radiation to be approximately  $c_g \approx -a$ , which gives the boundary condition  $U_\theta \approx 0$ .

For negative values of the parameter  $a$  (these solitons move towards the right-hand boundary), we impose therefore the condition  $U_\theta = 0$  at  $x = x_R$ . At the left-hand end we take  $U = U_\xi = U_{\xi\xi} = 0$  at  $x = x_L$ .

To illustrate the possible effects of different boundary conditions on the numerical solution, we display in Fig. 2 (right plot) the solution for a typical run on a moving uniform mesh with nonabsorbing and one with an absorbing boundary, again using the explicit solution as initial data. We see that using the nonabsorbing boundary conditions cause either numerical rounding errors or explicitly imposed noise on the initial solution, reflection at the right boundary (the noise or radiation reflects back into the domain as if the right boundary acts as a solid wall). With a transport or absorbing boundary condition this effect is almost negligible. It may be obvious that this effect is even more pronounced when using a fixed uniform mesh.

### 2.1.3. Numerical solution of the PDE

For the numerical solution of the time-dependent PDE (5) we use the method of lines, which consists of two steps. First, Eq. (5) and the boundary conditions are semidiscretized in the spatial direction using standard finite differences. For example, the fifth-order derivative is approximated by fourth-order

central differences:

$$u_{xxxxx,i} \approx \left[ -\frac{1}{6} u_{i+4} + \frac{3}{2} u_{i+3} - \frac{13}{3} u_{i+2} + \frac{29}{6} u_{i+1} - \frac{29}{6} u_{i-1} + \frac{13}{3} u_{i-2} - \frac{3}{2} u_{i-3} + \frac{1}{6} u_{i-4} \right] / h^5, \quad \text{with } h = \frac{x_R - x_L}{N - 1}, \quad (8)$$

where  $N$  denotes the number of spatial meshpoints. The lower-order spatial derivatives are treated similarly by fourth-order central differences. Discretizing all the terms in the spatial direction yields a large system of stiff ODEs. Since in the fifth-order derivative approximation a factor  $1/h^5$  appears, we note that this ODE system will be *very* stiff for small values of the meshsize  $h$ . In the second step an “appropriate” integration method has to be used to obtain the fully discrete numerical solution of the PDE in space and time. For this purpose, we use the numerical integrator DASSL (see [11]) which is specifically well suited to stiff systems. The integrator makes use of variable timestepping and variable order (up to order 5) of the underlying BDF methods. In DASSL we set the time tolerance to be  $\text{TOL} = 10^{-5}$ .

#### 2.1.4. Initial conditions

As initial conditions we take exact ES solutions, either obtained from the formula (4) or via accurate numerical integration of the ODE (3) plus a perturbation. We take a specific form of perturbation. Instead of starting with  $U|_{\theta=0}$  we take as initial solution

$$U|_{\theta=0}[1 + \rho(1 + A \sin(\omega\xi))], \quad (9)$$

where  $\rho$  is an “offset” parameter that determines the size and sign of the perturbation to the energy of the solitary wave. The results which follow were not found to be highly sensitive to the oscillatory part of the perturbation, and all the results below are presented for  $A = 1$  and frequency  $\omega = 0.5$ .

#### 2.1.5. Numerical results with the moving uniform mesh method

In Fig. 3 we show results for the case  $b = 0$  and  $\rho = 0$  (no perturbation of the initial exact solution) for an increasing number of meshpoints. It is clear from this picture that, in order to obtain accurate solutions with a nonadaptive method, we need to apply an enormous amount of meshpoints.  $N = 40\,001$  meshpoints are used in the continuation of our numerical experiments. In Figs. 4, 5 and 6, the time-dependent behaviour of the solution is depicted for  $b = 0$ , and different values of the offset parameter  $\rho$ . Fig. 4 ( $\rho = 0$ ; no perturbation of the initial solution) seems to indicate a stable behaviour of the explicit solution given by formula (4). However, if we take a look at Fig. 6 (with  $\rho = -0.01$ ; small negative energy perturbation) we see that the solution damps out quickly to a tiny positive skew pulse accompanied with an envelope solution that is moving to the right. If we add a small positive energy ( $\rho = +0.01$ ) instead, the perturbation remains “forever” (at least till  $t = 300$ ) at the right foot of the moving soliton (see Fig. 5). This interesting behaviour has been called semistability (see the introductory section) and can also be numerically simulated with the adaptive mesh method introduced in the next section.

## 2.2. An adaptive mesh method

The second method does not make use of the exact speed of the solitons, but re-arranges the spatial mesh point distribution in such a way that the spatial profile is resolved very accurately at every point of

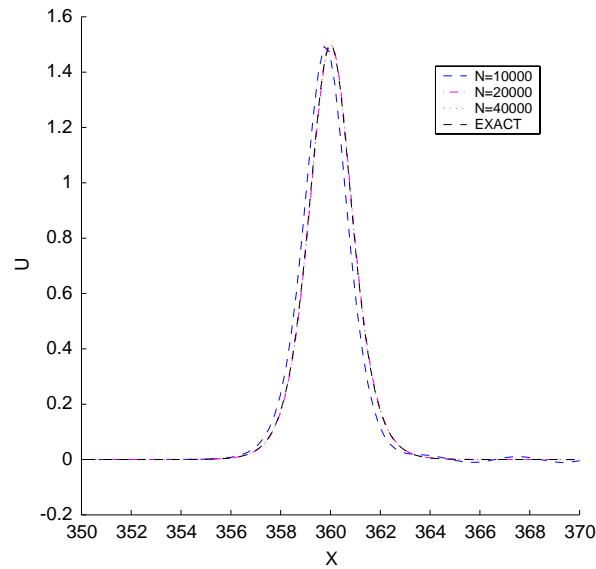


Fig. 3. Numerical solutions for the moving-uniform mesh method with  $\rho = 0$  (no initial perturbation) at  $t = 300$  (zoomed in around  $x = 360$ );  $N = 10\,001, 20\,001, 40\,001$  and exact solution,  $b = 0$ .

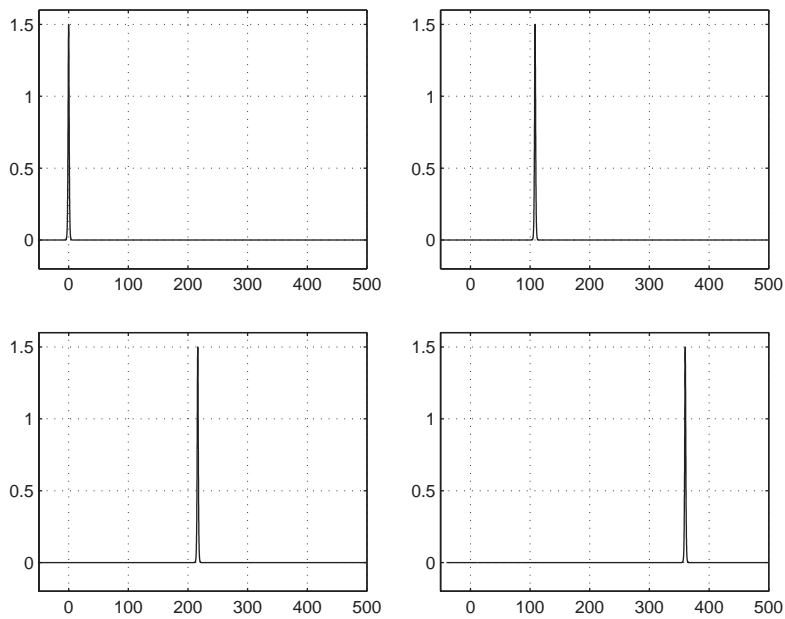


Fig. 4. Numerical solutions for the moving-uniform mesh method with  $\rho = 0$  (no initial perturbation) at  $t = 0, 90, 180, 300$ ;  $N = 40\,001, b = 0$ .

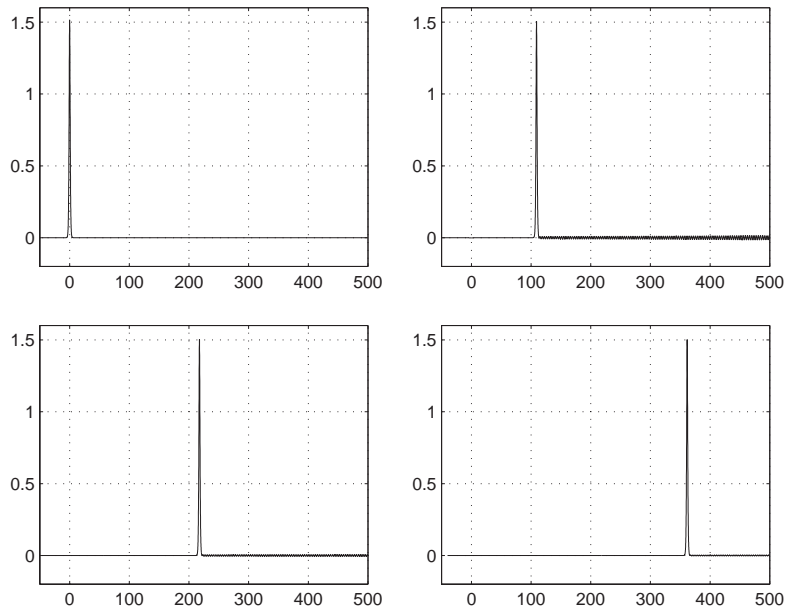


Fig. 5. Numerical solutions for the moving-uniform mesh method with  $\rho = 0.01$  (positive energy perturbation) at  $t = 0, 90, 180, 300$ ;  $N = 40\,001$ ,  $b = 0$ .

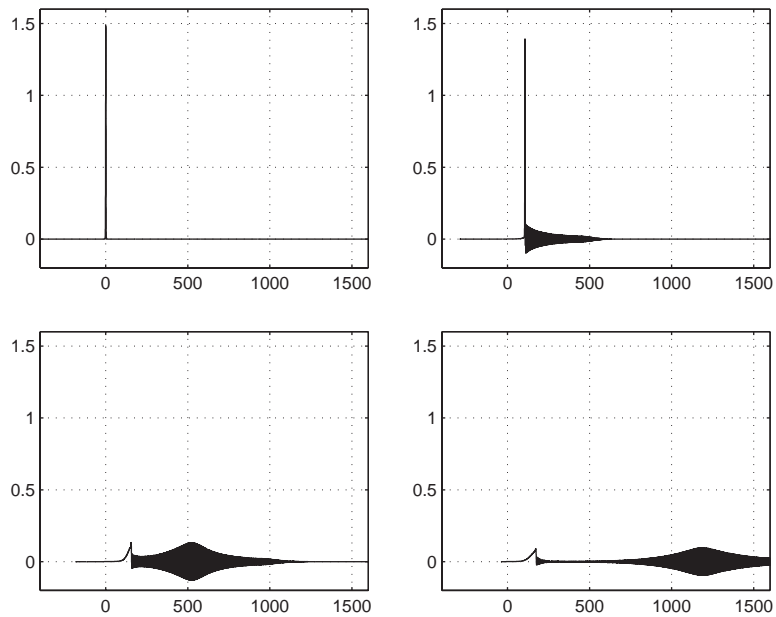


Fig. 6. Numerical solutions for the moving-uniform mesh method with  $\rho = -0.01$  (negative energy perturbation) at  $t = 0, 90, 180, 300$ ;  $N = 40\,001$ ,  $b = 0$ .

time. This so-called adaptive mesh refinement (AMR) algorithm equidistributes a given monitor function subject to constraints on the mesh regularity. Specifically, a spatial mesh  $x_i, i = 1, 2, \dots, N$ , is built so as to equidistribute a specified monitor function  $m(u)$ , i.e

$$\int_{x_{i-1}}^{x_i} m(u) \, dx = \int_{x_i}^{x_{i+1}} m(u) \, dx = p, \quad 2 \leq i \leq N - 1, \tag{10}$$

where  $p$  is a constant.

Various forms of monitor function, based on the solution arc-length or curvature, have been proposed. Here, an arc-length monitor function is used, i.e.

$$m(u) = \sqrt{\alpha + \|u_x\|_2^2}, \tag{11}$$

where  $\alpha > 0$  ensures that the monitor function is strictly positive and acts as a regularization parameter which forces the existence of at least a few nodes in flat parts of the solution.

The spatial derivatives of PDE (1) in Eulerian coordinates are approximated using finite difference approximations on nonuniform meshes [6]. The accuracy of the spatial derivative approximations and the stiffness of the semidiscrete system of differential equations are largely influenced by the regularity and spacing of the mesh points. This stresses the importance of limiting mesh distortion in such a way that

$$\frac{1}{K} \leq \frac{\Delta x_i}{\Delta x_{i-1}} \leq K, \quad 2 \leq i \leq N - 1, \tag{12}$$

where  $\Delta x_i = x_{i+1} - x_i$  is the local mesh spacing, and  $K$  is a constant.

To achieve such spatial regularization, a “monitor padding” procedure due to Kautsky and Nichols [8] is used here.

Time integration of the semidiscrete system of stiff ODEs is accomplished using the variable step, fifth-order, implicit Runge–Kutta solver RADAU5 [7]. Time integration is halted periodically, i.e. every  $N_{\text{adapt}}$  integration steps, to refine the spatial mesh. More details on the adaptive mesh method can also be found in [15].

### 3. Numerical simulations with the adaptive mesh

We now investigate the dynamics of slightly perturbed solitary and multihumped waves using the adaptive mesh method described in the previous section. Besides the dynamics of the solutions themselves, we will also monitor the temporal behaviour of three known invariants of this PDE model. The invariants are given by the following integrals:

Invariant 1 (conservation of mass for the water waves):  $I_1 := \int_{-\infty}^{\infty} u \, dx$ .

Invariant 2 (conservation of the horizontal momentum):  $I_2 := \int_{-\infty}^{\infty} u^2 \, dx$ .

Invariant 3 (conservation of the energy):  $I_3 := \int_{-\infty}^{\infty} [\frac{1}{15} u_{xx}^2 + \frac{1}{2} u^3 + \frac{1}{2} u_x^2 \{\frac{b}{2} - u\}] \, dx$ .

Integral  $I_1$  is trivially conserved. This follows directly from the fact that the PDE model can be written in the form  $u_t + X_x = 0$ ; see (2). Assuming that  $X \rightarrow \text{constant}$  as  $|x| \rightarrow \infty$  and integrating by parts

gives  $(d/dt) \int_{-\infty}^{\infty} u \, dx = 0$ . Since (1) is a Hamiltonian PDE, it also conserves  $I_2$ . Further, if we name the Hamiltonian  $\mathcal{H} = I_3$ , Eq. (2) is equivalent with

$$u_t = \mathcal{J}^{-1} \frac{\delta \mathcal{H}}{\delta u}, \tag{13}$$

with a skew-symmetric operator  $\mathcal{J}^{-1} = \partial/\partial x$ , i.e.  $\mathcal{J}^{-1} = -\mathcal{J} = \mathcal{J}^T$ . The variational derivative in (13) is given by

$$\frac{\delta \mathcal{H}}{\delta u} = \sum_{k=0}^{\infty} (-1)^k \left( \frac{d}{dx} \right)^k \frac{\partial \mathcal{H}}{\partial u_{kx}} = \frac{\partial \mathcal{H}}{\partial u} - \frac{d}{dx} \frac{\partial \mathcal{H}}{\partial u_x} + \frac{d^2}{dx^2} \frac{\partial \mathcal{H}}{\partial u_{xx}} - \dots \tag{14}$$

If we define the Poisson brackets

$$\{\mathcal{T}, \mathcal{S}\} = \int_{\Omega} \frac{\delta \mathcal{T}}{\delta u} \mathcal{J} \frac{\delta \mathcal{S}}{\delta u},$$

then it follows that  $\{\mathcal{T}, \mathcal{S}\} = -\{\mathcal{S}, \mathcal{T}\}$ . To show that  $\mathcal{H}$  is invariant, we work out the following relations (the function  $f$  is the integrand of  $I_3$ ):

$$\frac{d\mathcal{H}}{dt} = \frac{d}{dt} \int_{\Omega} f \, dx = \int_{\Omega} \left[ \frac{\partial f}{\partial u} u_t + \frac{\partial f}{\partial u_x} u_{tx} + \frac{\partial f}{\partial u_{xx}} u_{txx} + \dots \right] dx = \int_{\Omega} \frac{\delta \mathcal{H}}{\delta u} u_t \, dx = \{\mathcal{H}, \mathcal{H}\} = 0. \tag{15}$$

### 3.1. Embedded solitons ( $a < 0$ )

#### 3.1.1. Varying the parameter $b$ along the uppermost curve 1 in Fig. 1

For the case  $b = 0$ , we have seen that the moving uniform mesh is able to accurately describe different solution features, and particularly the semistability of the solitons. Numerical experiments with the fully adaptive mesh method confirm these results. In the nonperturbed case, efficient computation can be achieved with the following parameter values:  $\alpha = 0$ ,  $p = 0.0005$ ,  $K = 1.03$  and  $N_{\text{adapt}} = 1$ . The number of meshpoints then varies around 6500 (which is to be compared with the 40 001 points required by the moving uniform mesh). If less accuracy is required, the number of meshpoints can be reduced to about 1000 by increasing  $K$  up to 1.1.

When a positive or negative energy perturbation is added, the observations are essentially the same. In the case of a negative energy perturbation, we see that the solution damps out quickly to a tiny positive skew pulse accompanied with an envelope solution that is moving to the right. After some point of time, the PDE solution can be approximated asymptotically by (assuming  $u$  small and  $u_{5x}$  dominating)

$$u_t + \frac{2}{15} u_{xxxxx} = 0, \tag{16}$$

which can be interpreted in terms of similarity solutions and integrals of Airy-type functions. Looking at Fig. 6, we can estimate the group velocity of the envelope and compare it with the theoretical group velocity coming from an asymptotic dispersion relation. These two are in very good agreement.

In Figs. 7 and 8, runs for different (negative and positive)  $b$ -values (without noise) are depicted. These figures show both the evolution of the solution (upper graphs) and the evolution of the spatial mesh

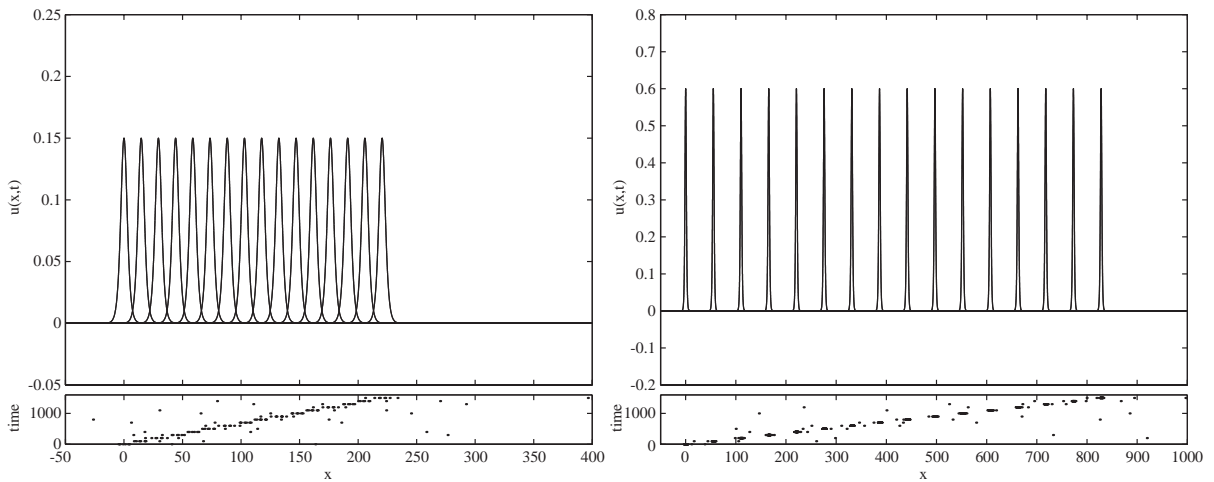


Fig. 7. Numerical solution with the adaptive mesh method in two different cases  $b = -0.45$  (left) and  $b = -0.30$  (right), at  $t = 0, 100, 200, \dots, 1500$ .

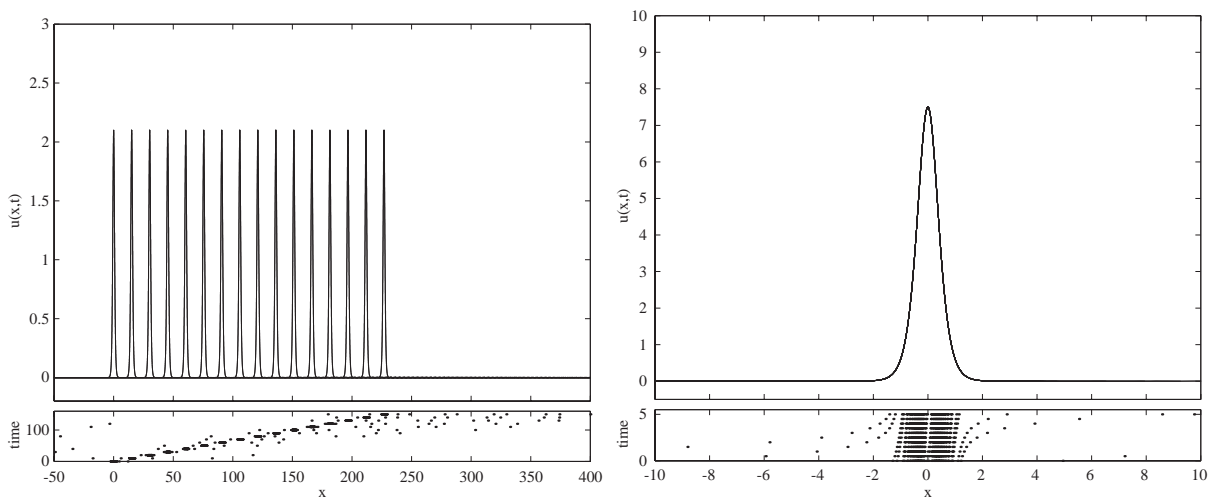


Fig. 8. Numerical solution with the adaptive mesh method in two different cases  $b = 0.2$  (left) at  $t = 0, 100, 200, \dots, 1500$ , and  $b = 2$  (right), at  $t = 0, 0.5, 1, \dots, 5$ .

(bottom graphs), which concentrate into the soliton. We observe that the numerical PDE solution seems to be stable for long periods of time. These observations are supported by runs where noise was added (just as for the  $b = 0$  situation earlier). However, computation is more demanding and delicate for positive  $b$ -values than for negative  $b$ -values. Fig. 8 shows that the spatial mesh not only follows the soliton, but also gets more and more densely populated along the right tail of the soliton. A closer look at the solution in this region shows spurious oscillations, which can be eliminated through the use of denser grids. However, the computational load increases rapidly, making such an analysis impractical. The situation

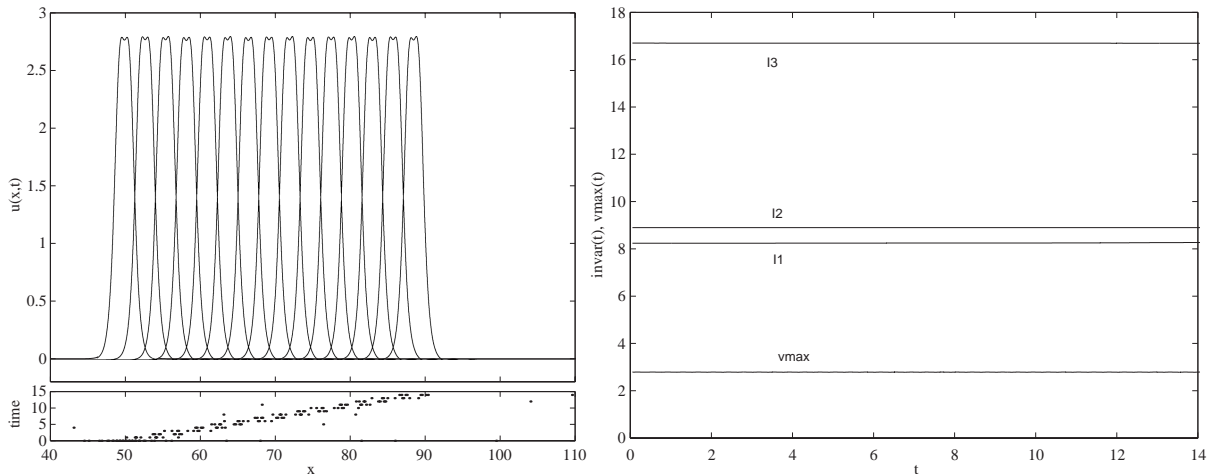


Fig. 9. Numerical solution (left), invariants  $I_1$ ,  $I_2$ ,  $I_3$  and soliton amplitude  $v_{\max}$  (right) with the adaptive mesh method in the case  $b = 0$ ,  $a = -2.747732$ , at  $t = 0, 1, 2, \dots, 14$ .

corresponding to  $b = 2$  is an exception, as it corresponds to a motionless soliton, which is relatively easy to capture with the adaptive mesh method.

### 3.2. Multihumped waves (along other curves 2–4 in Fig. 1)

We now consider solutions on the other curves represented in Fig. 1. Particularly, Fig. 9 shows the evolution of the solution corresponding to  $b = 0$  and  $a = -2.747732$ , i.e. a particular point on the second curve which corresponds to a “two-hump” soliton travelling from left to right. This solution is computed by the adaptive mesh method with the following parameter values:  $\alpha = 0$ ,  $p = 0.007$ ,  $K = 1.1$  and  $N_{\text{adapt}} = 1$ . About 930 mesh points are required. Fig. 9 also shows the evolution of the invariants  $I_1$ ,  $I_2$ ,  $I_3$ , as well as the soliton amplitude  $v_{\max}$ , which all remain constant (up to 3 significant digits). We also performed simulation runs with positive or negative energy perturbations, and the solution appears stable under both perturbations. Similar observations hold for the subsequent solution curves in Fig. 1. However, it is difficult to conclude about the stability of solutions on the fourth curve, i.e. negative energy perturbations generate an oscillatory behaviour of the peak of the soliton.

### 3.3. Multiple solitons ( $a > 0$ )

We now make some investigations for positive  $a$ -values, i.e. in the upper part of Fig. 1. In this case, the solution behaviour can be particularly intriguing. We first consider the parameter values  $b = 1.5$  and  $a = 2$ , and two different initial conditions. The first one is a “single soliton”, whose evolution is illustrated in Fig. 10 at  $t = 0, 1, \dots, 21$ . In addition, the figure shows the evolution of the invariants, which all remain constant on the considered time interval. The second one is a “double soliton” whose behaviour, illustrated in Fig. 11 at  $t = 0, 5, 6, \dots, 12$ , is quite complex and features several “phases”. Fig. 12 shows the evolution of the solution invariants on a somewhat longer time interval. These numerical solutions are again computed by the adaptive mesh method with  $\alpha = 0$ ,  $p = 0.007$ ,  $K = 1.1$  and  $N_{\text{adapt}} = 1$ . The

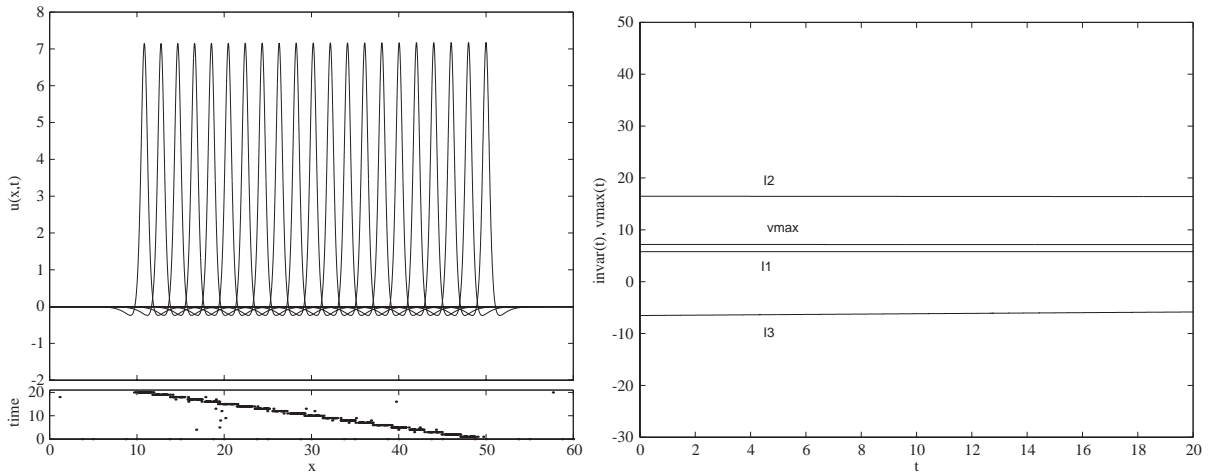


Fig. 10. “Single soliton” solution (left), invariants  $I_1, I_2, I_3$  and soliton amplitude  $v_{\max}$  (right) with the adaptive mesh method in the case  $b = 1.5, a = 2$ , at  $t = 0, 1, 2, \dots, 21$ .

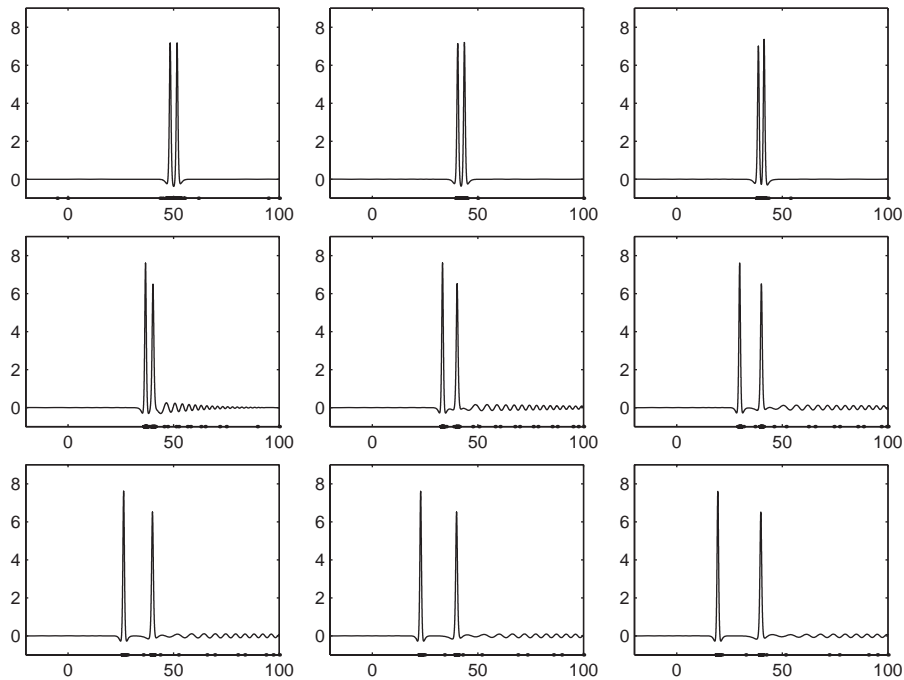


Fig. 11. “Double soliton” solution with the adaptive mesh method in the case  $b = 1.5, a = 2$ , at  $t = 0, 5, 6, \dots, 12$ .

number of mesh points is about 2500 in the first case, and varies between 4500 and 5500 in the second case. Simulation runs with positive and negative energy perturbations demonstrate the stability of these solutions. Finally, we consider  $b = 3$  and  $a = 2$ , and a “triple soliton” initial condition. Fig. 13 shows the solution evolution at  $t = 9, 10, \dots, 17$ , which is again quite intriguing.

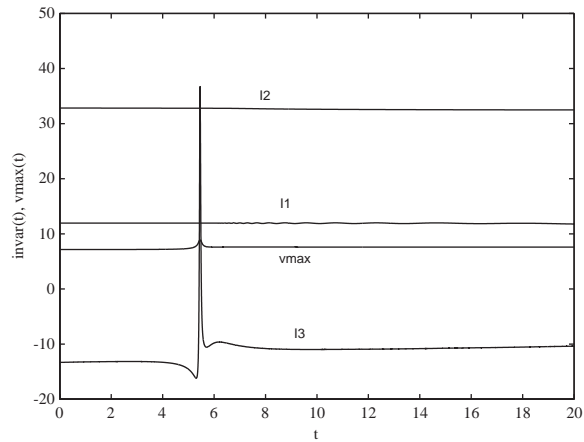


Fig. 12. “Double soliton” solution—invariants  $I_1$ ,  $I_2$ ,  $I_3$  and soliton amplitude  $v_{\max}$ .

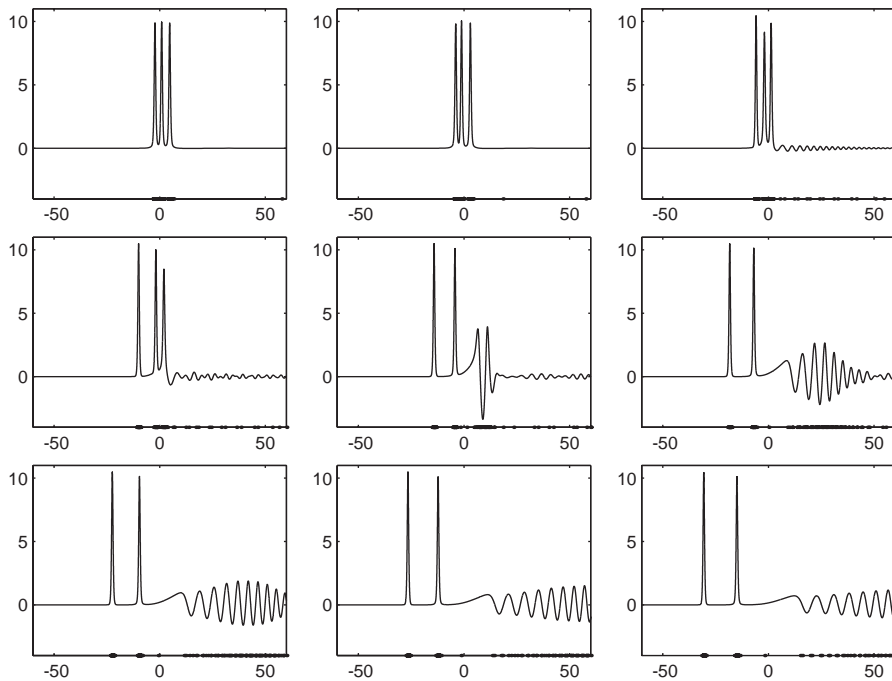


Fig. 13. “Triple soliton” solution with the adaptive mesh method in the case  $b = 3$ ,  $a = 2$ , at  $t = 9, 10, \dots, 17$ .

#### 4. Conclusions

In this paper, we have successfully applied moving and adaptive mesh methods for the numerical solution of an extended fifth-order KdV model describing (water) waves and solitons in the presence of surface tension. We have seen that a variety of solutions exist for which existence and stability properties

can be investigated numerically. Analytic and asymptotic theory would be needed to support the obtained numerical results. Particularly, eigenvalue computations could give more information about the stability of the different waves that have been computed.

## Acknowledgements

Paul Zegeling is grateful to the Joint Scientific Research Programme (Ref: JRP559, NWO: BR 61-438) for a travel grant to visit the UK. The authors would like to thank Alan Champneys for the interesting discussions regarding the fifth-order KdV model.

## References

- [1] A.R. Champneys, Codimension-one persistence beyond all orders of homoclinic orbits to singular saddle centres in reversible systems, *Nonlinearity* 14 (2002) 87–112.
- [2] A.R. Champneys, M.D. Groves, A global investigation of solitary wave solutions to a two-parameter model for water waves, *J. Fluid Mech.* 342 (1997) 199–229.
- [3] A.R. Champneys, B.A. Malomed, J. Yang, D.J. Kaup, “Embedded solitons”: solitary waves in resonance with the linear spectrum, *Physica D* 154 (2000) 340–354.
- [4] W. Craig, M.D. Groves, Hamiltonian long-wave approximations to the water-wave problem, *Wave Motion* 19 (1994) 367–389.
- [5] A. Doelman, T.J. Kaper, P.A. Zegeling, Pattern formation in the one-dimensional Gray–Scott model, *Nonlinearity* 10 (1997) 523–563.
- [6] B. Fornberg, Calculation of weights in finite difference formulas, *SIAM Rev.* 40 (1998) 685–691.
- [7] E. Hairer, G. Wanner, *Solving Ordinary Differential Equations II. Stiff and Differential-Algebraic Problems*, Springer, Berlin, 1991.
- [8] J. Kautsky, N.K. Nichols, Equidistributing meshes with constraints, *SIAM J. Sci. Statist. Comput.* 1 (1980) 499–511.
- [9] R. Kawahara, Oscillatory solitary waves in dispersive media, *J. Phys. Soc. Japan* 33 (1972) 260–264.
- [10] S. Kichenassamy, P.J. Olver, Existence and non-existence of solitary wave solutions to higher-order model evolution equations, *SIAM J. Math. Anal.* 23 (1992) 1141–1166.
- [11] L.R. Petzold, A description of DASSL: a differential/algebraic system solver, *IMACS Trans. Sci. Comput.* (1983) 65–68.
- [12] P. Saucez, A. Vande Wouwer, W.E. Schiesser, An adaptive method of lines solution of the Korteweg–de Vries equation, *Comput. Math. Appl.* 35 (1998) 13–25.
- [13] W.E. Schiesser, PDE Boundary Conditions from Minimum Reduction of the PDE, *Appl. Numer. Math.* 20 (1996) 171–179.
- [14] A. Vande Wouwer, P. Saucez, W.E. Schiesser, Some user-oriented comparisons of adaptive grid methods for partial differential equations in one space dimension, *Appl. Numer. Math.* 26 (1998) 49–62.
- [15] A. Vande Wouwer, P. Saucez, W.E. Schiesser (Eds.), *Adaptive Method of Lines*, Chapman & Hall/CRC, Boca Raton, 2001.
- [16] J. Yang, Dynamics of embedded solitons in the extended Korteweg–de Vries equations, *Stud. Appl. Math.* 106 (2001) 337–365.
- [17] J. Yang, B.A. Malomed, D.J. Kaup, Embedded solitons in second-harmonic-generating systems, *Phys. Rev. Lett.* 83 (1999) 1958–1961.
- [18] J. Yang, B.A. Malomed, D.J. Kaup, A.R. Champneys, Embedded solitons: a new type of solitary waves, *Maths. Comput. Simulation* 56 (2001) 585–600.
- [19] P.A. Zegeling,  $r$ -refinement for evolutionary PDEs with finite elements of finite differences, *Appl. Numer. Math.* 26 (1998) 97–104.
- [20] P.A. Zegeling, R. Keppens, Adaptive method of lines for magneto-hydrodynamic PDE models, in: A. Vande Wouwer, P. Saucez, W.E. Schiesser (Eds.), *Adaptive Method of Lines*, Chapman & Hall/CRC, Boca Raton, 2001.